Understanding Topological Defects in Fluidized Dry Active Nematics

Journal:	*Soft Matter*
Manuscript ID	SM-ART-09-2021-001405.R2
Article Type:	Paper
Date Submitted by the Author:	30-Dec-2021
Complete List of Authors:	Palmer, Bryce; Michigan State University Chen, Sheng; Michigan State University Govan, Patrick; Michigan State University, Engineering Yan, Wen; Flatiron Institute Gao, Tong; Michigan State University, Mechanical Engineering

SCHOLARONE™
Manuscripts

Journal Name

Understanding Topological Defects in Fluidized Dry Active Nematics

Bryce Palmer,[a‡] Sheng Chen,[a‡,e] Patrick Govan,[b] Wen Yan,[d] and Tong Gao [*a,c]

Dense assemblies of self-propelling rods (SPRs) may exhibit fascinating collective behaviors and anomalous physical properties that are far away from equilibrium. Using large-scale Brownian dynamics simulations, we investigate the dynamics of disclination defects in 2D fluidized swarming motions of dense *dry* SPRs (i.e., without hydrodynamic effects) that form notable local positional topological structures that are reminiscent of smectic order. We find the deformations of smectic-like rod layers can create unique polar structures that lead to slow translations and rotations of $\pm 1/2-$order defects, which are fundamentally different from the fast streaming defect motions observed in *wet* active matter. We measure and characterize the statistical properties of topological defects and reveal their connections with the coherent structures. Furthermore, we construct a bottom-up active-liquid-crystal model to analyze the instability of polar lanes, which effectively leads to defect formation between interlocked polar lanes and serves as the origin of the large-scale swarming motions.

1 Introduction

Collective dynamics of densely packed, self-propelling rods (SPRs), such as swarming of bacteria[1–3] and motor-driven biopolymers[4,5], can exhibit anomalous out-of-equilibrium physical properties. Of particular interest is understanding the so-called "active nematics" that feature fascinating orientational orders such as motile disclination defects[6–8]. In addition, the polar motions of aggregating SPRs may lead to eminent positional orders by breaking translational symmetry[9–11]. Compared to orientational orders that typically have myriad shapes and sizes, positional orders manifest as simple layered structures (e.g., smectic order) with a thickness of approximately one rod length. They are seldom found in *wet* systems wherein hydrodynamic effects bend and break alignment structures[4,12] and suppress phase transitions towards forming positional structures. Intriguing positional orders and structures are more often seen in *dry* SPR assemblies such as gliding bacteria colonies[13–15], where the short-range driving forces arise from friction, collision, or thermal fluctuations.

While understanding orientational orders and their

non-equilibrium transitions have been the focus of extensive studies, far less is known about positional orders. Quasi-steady, smectic-like patterns were created using phenomenological (e.g., Vicsek-type) continuum models[16–20]; however, these models cannot accurately resolve the nonlinear, anisotropic many-body collisions that essentially drive the phase transitions. On the other hand, direct particle simulations can reveal microscopic details, but performing large-scale simulations often requires scalable algorithms that simultaneously resolve collisions and thermal fluctuations. Their high computational cost significantly prevents particle simulations from being used in cross-scale studies. Although several simulation studies of dense SPRs captured the formation of various intriguing orientational and positional orders[21–25], there is a lack of physical understanding of their formation mechanisms and their precise connections with the emergent coherent structures.

In this work, we combine large-scale Brownian dynamics (BD) simulations and continuum modeling to uncover the dynamics and behaviors of topological defects in a "fluidized" state of active nematics composed of dense SPRs that undergo persistent swarming motions. Moreover, we capture the multiscale origin of the unstable dynamics and their quantitative relations between the defect dynamics. The paper is organized as follows. Section 2 is dedicated to the discrete particle simulations of SPRs in a periodic domain where we systematically explore the parameter space to examine the longtime dynamics. We identify and present typical defect dynamics, together with particle statistics. In Section 3, we perform stability analysis for a mean-field continuum model to illustrate the underlying mechanisms for polar-lane break up which eventually leads to

---

[a] *Department of Mechanical Engineering, Michigan State University, East Lansing, MI 48864.*

[b] *Department of Physics and Astronomy, Michigan State University, East Lansing, MI 48864.*

[c] *Department of Computational Mathematics, Science and Engineering, Michigan State University, East Lansing, MI 48864.*

[d] *Center for Computational Biology, Flatiron Institute, New York, NY 10010.*

[e] *Department of Biomedical Engineering, Yale University, West Haven, CT 06516.*

[*] *E-mail: gaotong@egr.msu.edu.*
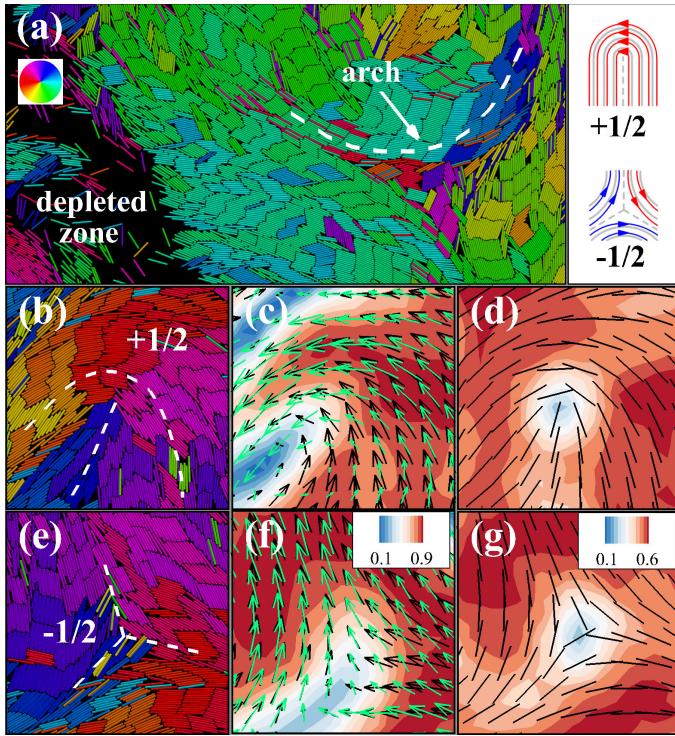
[‡] These authors contributed equally to this work.

Fig. 1 BD simulations reveal rich topological structures (Pe = 68, ϕ = 78%, γ = 10). (a) Examples of curved arches and depleted zones in a $30\ell \times 15\ell$ sub-domain. Schematics on the right: velocity distributions around $\pm 1/2-$order defects. (b-g) Zoom-in views of a $+1/2-$ (b-d) and a $-1/2-$order (e-g) defect. (c,f) Polarity q (black) and velocity u (green) vector fields superposed on the polar-order parameter $|q|$. (d,g) Nematic director field n superposed on the orientational-order parameter.

defect formation. Finally, we summarize and draw conclusions in Section 4.

2 BD Particle Simulation

In BD particle simulations, we consider each rod to have a spherocylinder shape with length ℓ and width b, and specified constant speed u_0 in the orientation direction p. To characterize the rod activity, here we define a dimensionless Péclet number Pe $= \frac{u_0 \eta_\parallel \ell}{k_B T}$ ($\eta_\parallel$ is the parallel drag coefficient). We initially distribute a monolayer of $N = 10^5 - 10^6$ rods homogeneously across across a $200\ell \times 200\ell$ planar domain with periodic boundary conditions. As rods start moving and interact, we solve the normal contact forces between frictionless rod-rod collisions at each time step using a geometrical constraint optimization method (see details in Ref.[26]), without employing any phenomenological (e.g., Lennard-Jones or Weeks-Chandler-Andersen) potentials.

We have explored the parameter space by systematically varying Pe, the aspect ratio $\gamma = \ell/b$, and the area fraction $\phi = N/L^2 \left(\pi b^2/4 + \ell b \right)$ and successfully resolved various types of collective motions, ranging from isolated clusters and homogeneous chaos to stable crystals[21,27,28]. Among them, the intriguing fluidized states (see Movie S1) are robustly captured for dense SPRs ($60\% < \phi < 85\%$) with a finite aspect ratio ($6 < \gamma < 30$) and high activity (Pe > 20), independent of the

initial configurations (e.g., either isotropic or nematically aligned). As highlighted in Fig. 1(a), we observe that the local positional structures exhibit both Smectic A and Smectic C-like orders, respectively corresponding to straight band and curved arch that are formed by interconnected rod layers with a thickness approximately one rod length. Meanwhile, aggregation of SPRs can cause large density fluctuations, leading to depleted zones with only a few isolated rods while the rod concentration in dense clusters remains approximately uniform.

Next, we reconstruct velocity u, director n, and polarity q vector fields on a uniform grid from the discrete particle data using the k-nearest neighbors algorithm[29]. We have successfully captured various types of defect motions, such as generation and annihilation, across the computation domain. The zoom-in views in Figs. 1(b,c) exhibit details of nematic and polar structures associated with the motile $\pm 1/2-$order disclination defects with sizes of multiple rod lengths, much larger than dislocations which are typically about one rod length. As shown in panels(b-d), the director field reveals a comet-like $+1/2-$order defect which typically carries curly bands that wrap around straight layers in the middle; while an inverted-Y shaped $-1/2-$order defect shown in panels(e-g) often sits between two adjacent polar groups that slide relative to each other. Moreover, panels(c) and (f) clearly show that the velocity vector field (green arrows) is highly correlated with the polarity field (black arrows), suggesting that the SPRs move approximately in the local alignment direction.

It has been well understood that in *wet* matter, defect motions may lead to coherent structures in the ambient flows. For example, a "streaming" $+1/2-$order defect, once born, will induce a localized jet in the direction of defect motion, between two oppositely signed vortices[7,12,15,30,31]. Nevertheless, as illustrated by the schematic on the right of Fig. 1(a), without hydrodynamic coupling with fluid flows, *dry* $\pm 1/2-$order defects may keep rotating as the rod layers located along the symmetry axes (marked by dashed grey lines) continuously tilt when being pushed by the surrounding polar bands or clusters, creating swirling velocity fields similar to Figs. 1(c) and (f). Indeed, as two examples shown in Figs. 2(a) and (b) where defect annihilation occurs respectively in the bulk and at the boundary, we clearly see rotational motions of both $\pm 1/2-$order defects when tracking the movements of defect symmetry axes (marked by yellow lines). Also, intriguingly, Movie S2 and S3 show that defect annihilation ends when the rod layers in the middle are eventually "released" due to uncurling of the traveling arch.

We then compute the global statistical properties of the defects and the corresponding velocity and orientation fields. As illustrated in Fig. 3(a), we identify $\pm 1/2$ defects via discrete contour integral of the director field[32,33]. By tracking their trajectories (marked by light green and purple lines) and symmetry axes (marked by dark green and purple lines), we obtain the distributions of the magnitude of defects' translational (V) and rotational (Ω) velocities as shown in panel(b). We find that, in contrast to the fast streaming behaviors in *wet* systems, here the $+1/2-$order defect moves as slowly as the $-1/2-$order defect, with the most probable speed only about 0.3 (the single
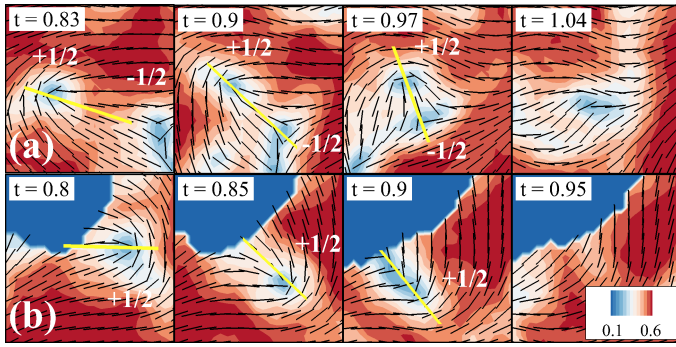
Fig. 2 Sequential snapshots of nematic director fields highlight defects' rotational motions (Pe = 68, ϕ = 78%, γ = 10). (a) Annihilation of a pair of $\pm 1/2$−order defects. (b) Annihilation of a $+1/2$−order defect at the boundary. The yellow lines mark the defects' symmetry axes.

rod moving speed is 1). The $+1/2$−order defects only move and rotate slightly faster than the $-1/2$−order ones because the polar, commet-like shape is less stable than the inverted-Y shape with its threefold symmetry. In panel(c), we calculate the two-point correlation function $g(r)$ for the defect core positions for the $(+1/2, +1/2)$, $(-1/2, -1/2)$, and $(+1/2, -1/2)$ pairs. It is seen that the defects of the same charge are statistically separated by greater than 10 rod lengths, while the oppositely-charged pairs may stay much closer due to generation and annihilation, as suggested by the peak around $r = 2$ on the $g_{(+1/2, -1/2)}$ curve.

Furthermore, we examine the statistical measurements of the swarming motions in the assembly and seek their connections with the topological defects. As shown in Fig. 3(d) where horizontally-aligned rods are distributed homogeneously at t = 0, defects start forming immediately after the system's mean enstropy $\langle \omega \rangle = \langle \frac{1}{2} |\nabla \times \boldsymbol{u}|^2 \rangle$ ($\langle \rangle$ represents a spatial average) reaches the maximum, corresponding to the strong shearing motions between interlocked polar lanes (see Movie S1). At quasi-steady states when $t > 0.6$, both the defect numbers and $\langle \omega \rangle$ plateau. The spatial correlation functions for the ensemble-averaged center-of-mass (C.O.M.) velocity (C_{uu}) and orientation (C_{pp}) of rods show a cut-off dimensionless length around 10, suggesting that the characteristic size of bulk "flow" is consistent with the separation distance between defects of the same charge shown in panel(c). In addition, in panel(f) we calculate the spectrums for the ensemble-averaged kinetic energy (E_k) and enstrophy (E_ω). Interestingly, on the length scale $2\pi/k$ close to the single-rod length, both measurements exhibit an asymptotic scaling close to k^{-4}, which hence suggests a similar trend for E_k but a faster decay for E_ω when compared to those reported in 2D *wet* systems [34,35].

To unveil the origins of the quasi-steady fluidized motions and to find their connections with the defect dynamics, we take a close look at the defect generation process. As shown in Figs. 4(a) and (b), generation of a pair of $\pm 1/2$−order defects typically occurs in between two oppositely oriented polar lanes with nematically aligned SPRs and move approximately unidirectionally. The process starts as a few misaligned rod layers rotate to become almost perpendicular to the lane and
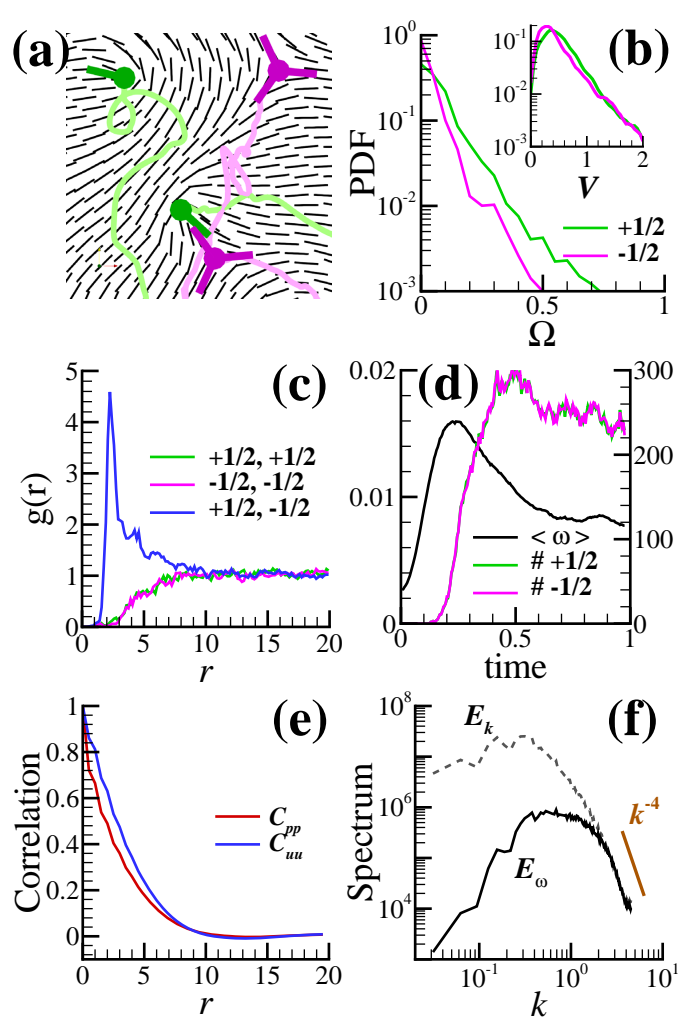

Fig. 3 Global statistical measurements (Pe = 68, ϕ = 78%, γ = 10). (a) Defect trajectories superposed on the director field. (b) Rotational (Ω) and translational (V) velocity magnitude distribution of $\pm 1/2$−order defects. (c) Two-point correlation function for defect core positions. (d) Time evolution of mean enstrophy $\langle \omega \rangle$ and defect numbers. (e) Rod C.O.M. velocity (C_{uu}) and orientation (C_{pp}) spatial correlation functions. (f) Kinetic-energy (E_k) and enstrophy (E_ω) spectrums.

then propagate away, which was also mentioned by Ref[22]. The moving front of this group keeps pushing the neighboring lane to form a curly arch, while the bottom continuously merges with the SPRs that run in the opposite direction, which eventually leads to the formation of a pair of $\pm 1/2$−order defects (see Movie S4). The two newly-born defects will start rotating after separation, seemingly being ripped apart by the shearing motions between the two lanes.

3 Continuum model

Evidently, the observed defect dynamics originate from the deformation and breakup of polar lanes. To gain further quantitative understandings, we construct a minimal continuum *dry* model for interactions between a polar lane wherein rods are sharply aligned in direction $\boldsymbol{q}_1$ and another small polar cluster pointing in direction $\boldsymbol{q}_2$, where $\boldsymbol{q}_{1,2}$ are two unit vectors (see schematic in Fig. 5(a)). We emphasize that although this
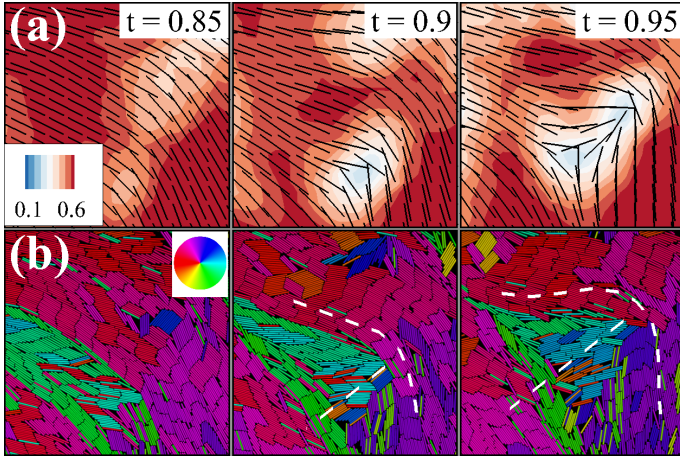
Fig. 4 Sequential snapshots of (a) the director field and (b) rendered images of rod distribution in a polar lane that bends and break ($Pe = 68$, $\phi = 78\%$, $\gamma = 10$).
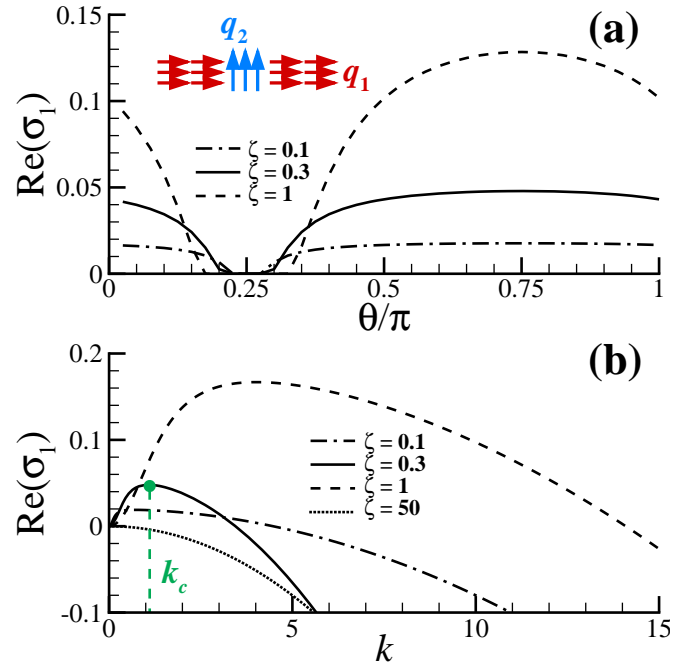

Fig. 5 The real part of the growth rate $\mathrm{Re}(\sigma_1)$ as a function of the wave-angle θ (a) and wavenumber k (b) for the perpendicular case (case I), when varying ζ and fixing $c_1^{(0)} = 0.9$, $c_2^{(0)} = 0.1$, $d = 0.005$. In panel(b), we fix the wave-angle $\theta_c = 3\pi/4$.

phenomena is somewhat reminiscent of the classical Kelvin-Helmholtz instability occurring between two fluids, here we are not intended to make connections to any phenomenological hydrodynamic models.

To begin with, we employ a probability distribution function (PDF) $\Psi(\boldsymbol{x}, \boldsymbol{p}, t)$ in terms of the rod's C.O.M. position $\boldsymbol{x}$ and orientation $\boldsymbol{p}$. The PDF satisfies the Smoluchowski equation[36]

$$\frac{\partial \Psi}{\partial t} + \nabla \cdot (\dot{\boldsymbol{x}}\Psi) + \nabla_p \cdot (\dot{\boldsymbol{p}}\Psi) = 0 \tag{1}$$

where ∇ is the regular spacial gradient operator and $\nabla_p = (\mathbf{I} - \boldsymbol{pp}) \cdot \partial/\partial \boldsymbol{p}$ is the orientational gradient operator on the unit sphere. The two conformational fluxes $\dot{\boldsymbol{x}}$ and $\dot{\boldsymbol{p}}$ using local slender-body theory as

$$\dot{\boldsymbol{x}} = \boldsymbol{p} - d\nabla(\ln \Psi), \tag{2}$$

$$\dot{\boldsymbol{p}} = -\nabla_p U_s, \tag{3}$$

where d is an effectively translational diffusion coefficient. Here $U_s = -\zeta(\mathbf{D} : \boldsymbol{pp})$ is the so-called Maier-Saupe potential that effectively produces a mean-field torque to enforce local alignment, with ζ a strength coefficient and $\mathbf{D} = \int_p \boldsymbol{pp}\Psi d\boldsymbol{p}$ the second-moment tensor[37]. Equations (2)-(3) state that an individual SPR can move along the $\boldsymbol{p}$−direction when subject to thermal fluctuations and can simultaneously rotate to align with the neighboring rods via steric interactions. Note that we also neglect the rotational diffusion by assuming the steric interactions dominate the rod's rotation in dense assemblies.

We assume a bi-directional form of Ψ for a main group of sharply aligned rods pointing in the $\boldsymbol{q}_1$−direction and a small polar cluster pointing in the $\boldsymbol{q}_2$−direction, such that

$$\Psi(\boldsymbol{x}, \boldsymbol{p}, t) = c_1(\boldsymbol{x}, t)\delta(\boldsymbol{p} - \boldsymbol{q}_1) + c_2(\boldsymbol{x}, t)\delta(\boldsymbol{p} - \boldsymbol{q}_2) \tag{4}$$

where $c_1 > c_2$, and δ is a Dirac delta function. Hence the Maier-Saupe potential can be written as

$$\mathbf{D} = c_1\boldsymbol{q}_1\boldsymbol{q}_1 + c_2\boldsymbol{q}_2\boldsymbol{q}_2. \tag{5}$$

which is then substituted into Eq. (3) to calculate the zeroth and the first moment of Eq. (1). After performing integration by parts on two hemispheres in the $\boldsymbol{p}$ space, it is straightforward to derive the coarse-grained equations for concentration $c_{1,2}$ and polarity vector $\boldsymbol{q}_{1,2}$[38]

$$\frac{\partial c_1}{\partial t} + \nabla \cdot (c_1\boldsymbol{q}_1) = d\Delta c_1, \tag{6}$$

$$\frac{\partial c_2}{\partial t} + \nabla \cdot (c_2\boldsymbol{q}_2) = d\Delta c_2, \tag{7}$$

$$\frac{\partial \boldsymbol{q}_1}{\partial t} + \boldsymbol{q}_1 \cdot \nabla \boldsymbol{q}_1 - 2\zeta c_2(\boldsymbol{q}_1 \cdot \boldsymbol{q}_2)[\boldsymbol{q}_2 - \boldsymbol{q}_1(\boldsymbol{q}_1 \cdot \boldsymbol{q}_2)] = d\Delta \boldsymbol{q}_1, \tag{8}$$

$$\frac{\partial \boldsymbol{q}_2}{\partial t} + \boldsymbol{q}_2 \cdot \nabla \boldsymbol{q}_2 - 2\zeta c_1(\boldsymbol{q}_1 \cdot \boldsymbol{q}_2)[\boldsymbol{q}_1 - \boldsymbol{q}_2(\boldsymbol{q}_1 \cdot \boldsymbol{q}_2)] = d\Delta \boldsymbol{q}_2. \tag{9}$$

To perform linear stability analysis, we adopt asymptotic expansions about the base-state equilibrium solutions, denoted by superscript "(0)",

$$c_{1,2} = c_{1,2}^{(0)} + \varepsilon c_{1,2}', \tag{10}$$

$$\boldsymbol{q}_{1,2} = \boldsymbol{q}_{1,2}^{(0)} + \varepsilon \boldsymbol{q}_{1,2}' \tag{11}$$

where perturbation variables are denoted by superscript "′". At the zeroth order $O(1)$, it is easy show that the admissible equilibrium solutions are

$$c_1^{(0)} = 1 - c_2^{(0)} = const, \quad \boldsymbol{q}_1^{(0)} = \hat{\boldsymbol{e}}_x, \quad \boldsymbol{q}_2^{(0)} = \hat{\boldsymbol{e}}_y, \quad \text{(case I)} \tag{12}$$

and

$$c_1^{(0)} = 1 - c_2^{(0)} = const, \quad \boldsymbol{q}_1^{(0)} = \hat{\boldsymbol{e}}_x, \quad \boldsymbol{q}_2^{(0)} = -\hat{\boldsymbol{e}}_x, \quad \text{(case II)} \quad (13)$$

At the order of $O(\varepsilon)$, we adopt a plane-wave decomposition and express the disturbance solutions as $c'(\boldsymbol{x},t) = \tilde{c}(\boldsymbol{k}) \exp(i\boldsymbol{k}\cdot\boldsymbol{x} + \sigma t)$ and $\boldsymbol{q}'(\boldsymbol{x},t) = \tilde{\boldsymbol{q}}(\boldsymbol{k}) \exp(i\boldsymbol{k}\cdot\boldsymbol{x} + \sigma t)$ with wave-vector $\boldsymbol{k} = k(\cos\theta, \sin\theta)$ and wave-angle $\theta \in [0,\pi)$ measured with respect to $\boldsymbol{q}_1^{(0)}$. This leads to a linear system from which we can solve the eigenvalue problems to obtain the real part of the growth rate $\text{Re}(\sigma_1)$ for the polar lane. For case I where two near-perpendicular groups interact, the growth rate being analytically derived as

$$\sigma_1 = \zeta - \frac{ik}{\sqrt{2}} \sin\left(\theta + \frac{\pi}{4}\right) - dk^2 -$$

$$\sqrt{\left[\zeta - \frac{ik}{\sqrt{2}} \sin\left(\theta + \frac{\pi}{4}\right)\right]^2 + \frac{k^2}{2} \sin(2\theta) + 2i\zeta k \left[\cos(\theta) c_1^{(0)} + \sin(\theta) c_2^{(0)}\right]}.$$

$$(14)$$

As shown in Fig. 5, we fix $\boldsymbol{q}_1^{(0)} = \hat{\boldsymbol{e}}_x$ to be horizontal and $d = 0.005$, and then vary ζ over a wide range $(O(10^{-1}) - O(10^2))$. We find instabilities can occur (i.e., $\text{Re}(\sigma_1) > 0$) when $\boldsymbol{q}_2^{(0)}$ points vertically, which is consistent with the numerical observations in Fig. 4, where the small group always moves approximately perpendicular to the polar lane. As shown in Fig. 5(a), the real part $\text{Re}(\sigma_1)$ of Eq. (14) reaches the maximum value at the critical wave-angle $\theta_c = 3\pi/4$. When fixing $\theta = \theta_c$, the corresponding $\text{Re}(\sigma_1) - k$ curves are shown panel(b). When ζ is specified, the instability appears to be of finite-wavelength, with the maximum $\text{Re}(\sigma_1)$ occurring at a critical wavenumber $k_c > 0$. When choosing ζ close to 0.3 (measured for dense passive Brownian rods with a finite aspect ratio[39]), we measure k_c to be approximately 1 (i.e., one rod length) with the characteristic length scale $\ell_c = 2\pi/k_c$ about 6, close to the measured characteristic length about 10 in Fig. 3 (c) and (e). Moreover, the model predicts that instabilities can be significantly suppressed when $\zeta \to 0$ or $\zeta \to \infty$. Since ζ measures the combined effects of aspect ratio γ and concentration ϕ[37,39], our analysis essentially indicates that such fluidized states won't occur for dilute and short-rod assemblies where the dynamics tend to be more homogeneous, nor do they happen for densely-packed assemblies of high aspect-ratio SPRs wherein polar lanes are much more stable, corresponding to large k_c and hence $\ell_c \ll 1$. These findings agree with numerical results from previous studies[23,27]. For case II where two groups are approximately anti-parallel, the growth rate can be derived as

$$\sigma_1 = -\zeta - dk^2 \pm \sqrt{\zeta^2 - k^2\cos^2(\theta) - 2ik\zeta\left(c_1^{(0)} - c_2^{(0)}\right)\cos(\theta)}, \quad (15)$$

which directly shows $\text{Re}(\sigma_1) \leq 0$, and hence suggests that the cases of two anti-parallel groups are always stable.

4   Conclusion

To summarize, we use large-scale BD simulations to resolve fluidized swarming motions of dense *dry* SPR assemblies. We demonstrate that, even without hydrodynamic effects, local interactions of active smectic-like structures may deform the orientation field in a long-range fashion, leading to rich defect dynamics and large-scale swarming motions. In particular, we find the $\pm1/2-$order defects in *dry* matter are born between two relative sliding polar lanes and exhibit significant rotations afterwards, owing to their unique polar structures. We expect these findings to provide new insights into the multiscale origin of dynamics in non-equilibrium soft condensed systems.

Conflicts of interest

There are no conflicts to declare.

Acknowledgements

Notes and references

1 A. Sokolov, I. Aranson, J. Kessler and R. Goldstein, *Phys. Rev. Lett.*, 2007, **98**, 158102.

2 H. Zhang, A. Be'er, E. Florin and H. Swinney, *Proc. Natl. Acad. Sci.*, 2010, **107**, 13626–13630.

3 J. Dunkel, S. Heidenreich, K. Drescher, H. Wensink, M. Bär and R. Goldstein, *Phys. Rev. Lett.*, 2013, **110**, 228102.

4 T. Sanchez, D. Chen, S. DeCamp, M. Heymann and Z. Dogic, *Nature*, 2012, **491**, 431–434.

5 R. Zhang, N. Kumar, J. Ross, M. Gardel and J. de Pablo, *Proc. Natl. Acad. Sci.*, 2018, **115**, E124–E133.

6 M. Marchetti, J. Joanny, S. Ramaswamy, T. Liverpool, J. Prost, M. Rao and R. Simha, *Rev. Mod. Phys.*, 2013, **85**, 1143–1189.

7 M. Shelley, *Annu. Rev. Fluid Mech.*, 2016, **48**, 487–506.

8 A. Doostmohammadi, J. Igné-Mullol, J. Yeomans and F. Sagués, *Nat. Commun.*, 2018, **9**, 3246.

9 T. Adhyapak, S. Ramaswamy and J. Toner, *Phys. Rev. Lett.*, 2013, **110**, 118102.

10 L. Chen and J. Toner, *Phys. Rev. Lett.*, 2013, **111**, 088701.

11 P. Romanczuk, H. Chaté, L. Chen, S. Ngo and J. Toner, *New J. Phys.*, 2016, **18**, 063015.

12 T. Gao, R. Blackwell, M. Glaser, M. Betterton and M. Shelley, *Phys. Rev. Lett.*, 2015, **114**, 048101.

13 E. Ben-Jacob, A. Finkelshtein, G. Ariel and C. Ingham, *Trends Microbiol.*, 2016, **24**, 257–269.

14 F. Beroz, J. Yan, B. Sabass, H. A. Stone, B. L. Bassler, N. S. Wingreen and Y. Meir, *Nat. Phys.*, 2018, **14**, 954–960.

15 O. J. Meacock, A. Doostmohammadi, K. R. Foster, J. M. Yeomans and W. M. Durham, *Nat. Phys.*, 2021, **17**, 205–210.

16 T. Vicsek, A. Czirók, E. Ben-Jacob, I. Cohen and O. Shochet, *Phys. Rev. Lett.*, 1995, **75**, 1226–1229.

17 K. Nagai, Y. Sumino, R. Montagne, I. Aranson and H. Chaté, *Phys. Rev. Lett.*, 2015, **114**, 168001.

18 A. Solon, H. Chaté and J. Tailleur, *Phys. Rev. Lett.*, 2015, **114**, 068101.

19 A. Patelli, I. Djafer-Cherif, I. Aranson, E. Bertin and H. Chaté, *Phys. Rev. Lett.*, 2019, **123**, 258001.

20 S. Saha, J. Agudo-Canalejo and R. Golestanian, *Phys. Rev. X*, 2020, **10**, 041009.

21 Y. Yang, V. Marceau and G. Gompper, *Phys. Rev. E*, 2010, **82**, 031904.

22 S. R. McCandlish, A. Baskaran and M. F. Hagan, *Soft Matter*, 2012, **8**, 2527–2534.

23 X. Shi and Y. Ma, *Nat. Commun.*, 2013, **4**, 3013.

24 M. C. Bott, F. Winterhalter, M. Marechal, A. Sharma, J. M. Brader and R. Wittmann, *Phys. Rev. E*, 2018, **98**, 012601.

25 R. Großmann, I. Aranson and F. Peruani, *Nat. Commun.*, 2020, **11**, 5365.

26 W. Yan, H. Zhang and M. Shelley, *J. Chem. Phys.*, 2019, **150**, 064109.

27 X. Shi and H. Chaté, *arXiv:1807.00294*, 2018.

28 M. Bär, R. Großmann, S. Heidenreich and F. Peruani, *Annu. Rev. Cond. Matter Phys.*, 2020, **11**, 441–466.

29 G. R. Terrell and D. W. Scott, *Ann. Statist.*, 1992, **20**, 1236–1265.

30 L. Giomi, M. Bowick, X. Ma and M. Marchetti, *Phys. Rev. Lett.*, 2013, **110**, 228101.

31 H. Li, X. Shi, M. Huang, X. Chen, M. Xiao, C. Liu, H. Chaté and H. P. Zhang, *Proc. Natl. Acad. Sci.*, 2019, **116**, 777–785.

32 K. B. Hoffmann and I. F. Sbalzarini, *Phys. Rev. E*, 2021, **103**, 012602.

33 A. J. Vromans and L. Giomi, *Soft Matter*, 2016, **12**, 6490–6495.

34 L. Giomi, *Phys. Rev. X*, 2015, **5**, 031003.

35 J. Urzay, A. Doostmohammadi and J. Yeomans, *J. Fluid Mech.*, 2017, **822**, 762–773.

36 M. Doi and S. Edwards, *The theory of polymer dynamics*, Oxford University Press, USA, 1988.

37 W. Maier and A. Saupe, *Zeit. Nat. Teil A*, 1958, **13**, 564.

38 T. Gao, R. Blackwell, M. Glaser, M. Betterton and M. Shelley, *Phys. Rev. E*, 2015, **92**, 062709.

39 S. Chen, W. Yan and T. Gao, *Phys. Rev. E*, 2020, **102**, 012608.